The crustal deformation mechanism of southern Chuandian block: constrained by S wave velocity and its azimuthal anisotropy

Zaiji Gao[1,2], Ya Sun[1,2]*, Jiwen Huang[1,2] and Qiu Li[1,2]

Abstract

We construct the 3D Shear wave velocity and azimuthal anisotropy images in the southern Chuandian block using phase velocity dispersion of Rayleigh wave in the period of 5–45 s. The images show two extensive low-velocity zones with a depth range of 20–40 km. The west range of the low-velocity extends from the Lijiang-Xiaojinhe fault to the Red River fault, while its east range follows along the Xiaojiang fault. Two ranges of low velocities are merged at the southern inner belt of the Emeishan Large Igneous Provinces (ELIP). The observed fast directions of azimuthal anisotropy are consistent with the extension of low-velocity ranges at the lower crust. The findings reveal the presence of two potential weak channels in the lower crust, characterized by low-velocity zones, which align with the hypothesis of lower crustal flow. Meanwhile, the crust around the inner belt of ELIP exhibits a high-velocity body characterized by a northeast-trending and counter-clockwise azimuthal anisotropy. Combined with geological data, we attribute the high S-velocity to a mafic–ultramafic magma reservoir of the ELIP, which blocks the continuity of crustal flow within the southern Chuandian block, thus dividing the lower crustal flow into two branches. Additionally, we also find the fast directions of azimuthal anisotropy above 20 km align well with the strike-slip fault orientations. The above research results indicate that the crustal deformation in the southern Chuandian block is likely attributed to the joint action of the two deformation mechanisms. One involves a lower crustal flow model, while the other entails rigid extrusion controlled by the deep-seated, large-scale strike-slip faults in the upper crust.

Keywords Southern Chuandian block, Shear wave velocity, Shear wave azimuthal anisotropy, Lower crustal flow, Rigid extrusion

Introduction

The southern Chuandian block is located at the junction of the Yangtze Craton and the southeast margin of the Tibetan Plateau (SE Tibet). It shows a long-wavelength margin with a gently sloping surface, different from the other steep margins of the Tibetan Plateau. It comprises most of Yunnan and part of the Sichuan Basin and Guizhou Province in southwest China (Fig. 1). Due to the N–S ongoing collision of the Indian and Eurasian plates since ~ 50 Ma, the topography and lithosphere structure of the Tibetan plateau have experienced enormous deformation. Large and deep faults and intense seismic activity are widely distributed in this region. Then, this region is an ideal place for understanding the deformation and uplift mechanism of the Tibetan Plateau, the rheological properties of materials within the continental plate, and the tectonic setting of intense earthquake preparation.

Two different models have been proposed to explain the lithospheric deformation of SE Tibet. One is the lower crustal flow (Royden et al. 1997), which deems that the

*Correspondence:
Ya Sun
sunya_seis@csu.edu.cn
[1] School of Geosciences and Info-Physics, Central South University, Changsha 410083, China
[2] Key Laboratory of Metallogenic Prediction of Nonferrous Metals and Geological Environment Monitoring, Central South University, Ministry of Education, Changsha 410083, China
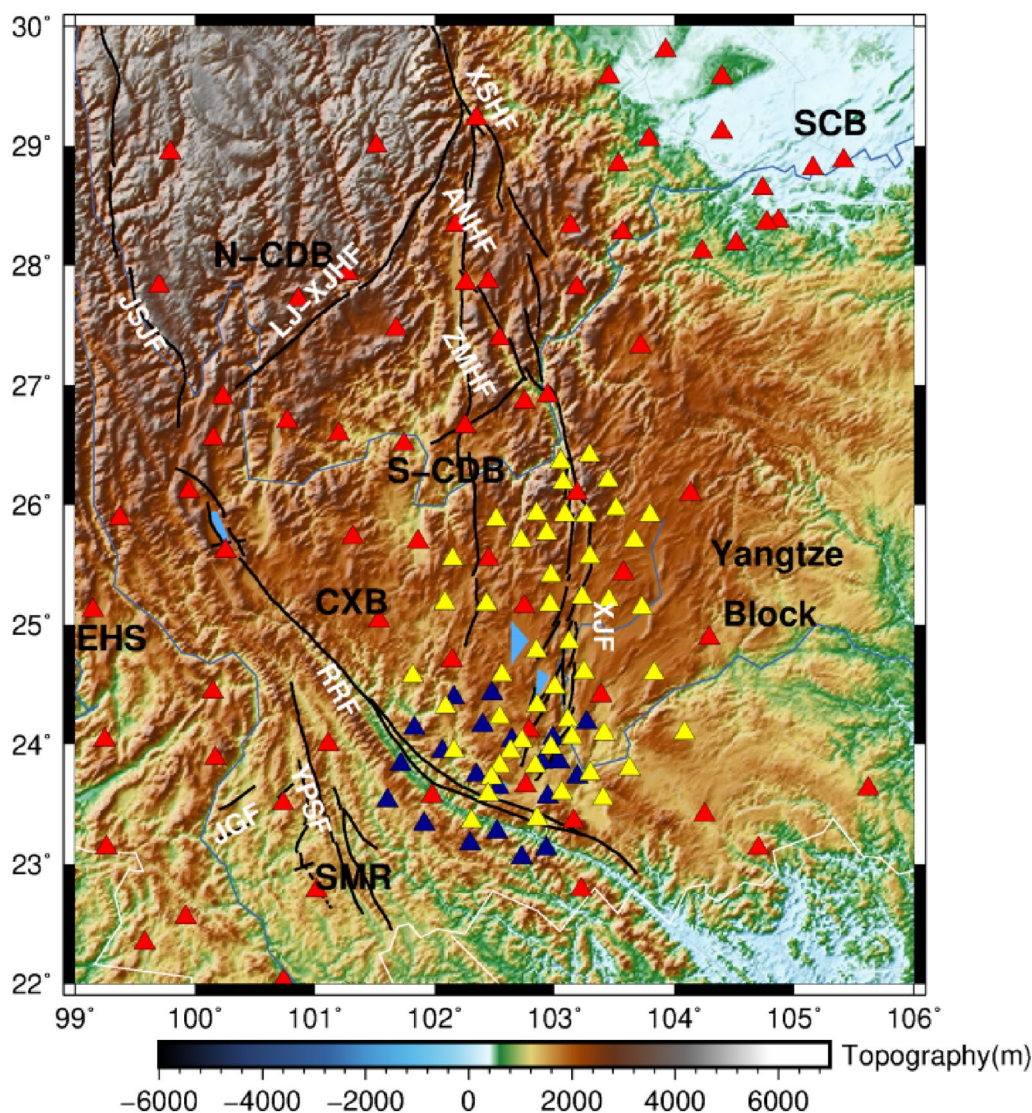
Gao *et al. Geoscience Letters*   (2024) 11:40

Page 2 of 19

Fig. 1 Distribution diagram of the stations. The red triangles represent the national permanent stations. The yellow triangles represent the broad-band mobile stations of the Xiaojiang fault zone. The blue triangles refer to independently distributed wide-band mobile seismic stations. The black lines represent the faults in the region. N-CDB: the northern Chuandian block; S-CDB: The south part of the Chuandian block; CXB: Chuxiong Basin; SCB: Sichuan Basin; EHS: East Himalayan block; SMR: the Simao block; JSJF: Jinshajiang Fault; LJ-XJH: Lijiang-Xiaojinhe fault; XSHF: Xianshuihe fault; ANHF: Anninghe fault; ZMHF: Zemuhe fault; XJF: Xiaojiang fault; RRF: Red River fault; YPSF: Yingpanshan fault; JGF: Jinggu fault

surface is uplifted by the material flow in the lower crust and causes crustal thickening. The other model is the lateral extrusion within the lithosphere along the large and deep faults (Tapponnier et al. 1982). For the crustal channel flow model, low viscosity and soft materials are believed to extend from the central Tibetan Plateau to SE Tibet. This results in east–west extension and the clockwise rotation to NW–SE extension with the decoupled deformation of the crust and mantle lithosphere. In contrast, the primary deformation for the lateral extrusion model is confined to the large and deep strike-slip faults

within the lithosphere. The crust and mantle lithosphere deformation is coherent inside the block. Both models are partly supported by geological data (Clark et al. 2005; Schoenbohm et al. 2006).

The lithospheric structure in SE Tibet has been investigated by geophysical studies (e.g., Yao et al. 2008, 2010; Bao et al. 2015; Liu et al. 2019; Chen et al. 2017). For example, surface wave images (Yao et al. 2005, 2008), joint inversion of Rayleigh wave and body wave data (Yang et al. 2023; Huang et al. 2010), and regional large-scale seismic images revealed that low-speed anomalies

are widely spread in the lower crust in SE Tibet (Yao et al. 2005, 2008) and extend to the southern Chuandian block (Lei et al. 2009; Yang et al. 2010). Xu et al. (2007) proposed that the distribution of these low-speed anomalies is heterogeneous and discontinuous in the Chuandian block. A joint inversion of receiver functions and surface wave showed only two ranges of low-velocity anomalies distributed in the depth range of 20–30 km (Wang and Gao 2014; Bao et al. 2015; Wu et al. 2016; Chen et al. 2016; Bao et al. 2015; Liu et al. 2021a). Furthermore, Magnetotelluric sounding profiles (Bai et al. 2010; Li et al. 2019a, b) showed that two low-resistivity layers spread around SE Tibet along the large strike-slip faults, such as the Xiaojiang fault and the Red River fault. The above studies generally support the model of the middle and lower crust flow in the Tibetan Plateau and believe that there may be a channel for the southeast materials flow from the Tibetan Plateau to Yunnan region (Wu et al. 2016; Bao et al. 2015; Liu et al. 2019).

The Rayleigh wave tomography showed that the low-velocity anomalies only spread around the Red River fault and its west side in the lower crust, and are rare in the southern Xiaojiang fault zone (Wu et al. 2019). However, Zhang et al. (2020) found significant low-speed anomalies around the Xiaojiang fault and its eastern side, which are not connected to the low-speed anomalies in the northern Chuandian region. They considered that these low-speed anomalies might be caused by crustal thickening, which leads to plastic deformation or even partial melting of the felsic material in the lower crust, unrelated to the lower crustal flow (Zhang et al. 2020). Although the lateral spatial extent and velocity magnitude of low-velocity zones were observed by different studies in this region, due to the limitations in the applied imaging methods and the spatial availability of stations, the distribution and connectivity of low-velocity zones of the Chuandian area are still controversial, especially in the Xiaojiang fault zone and the intersection of the Xiaojiang fault and Red River fault zone. Thus, the refined seismic wave structure is necessary based on the dense seismic stations in this complex geological area.

On the other hand, Seismic anisotropy has significance in indicating the lattice and shape-preferred orientation of mineral crystals and cracks under strain/stress, respectively (Savage 1999). It was widely used to detect crustal or mantle deformation. The Moho Ps splitting suggests significant crustal anisotropy with the fast direction of SE–NW under SE Tibet (Sun et al. 2012; Yang et al. 2010; Xu et al. 2007), which supported the lower crust flow model hypothesis extended from the Tibetan Plateau. However, Han et al. (2017) found a coherent deformation in the whole crust in this region based on the GPS and Ps splitting, which support the rigid block model within the crust along the significant deep strike-slip fault. Ps splitting only reflects the average anisotropy of the crust, while the SKS splitting has a low resolution in the vertical direction. SKS spitting cannot separate whether anisotropy comes from the crust or the upper mantle. Azimuthal anisotropy retrieved from surface waves can constrain deformation patterns in different crustal depths, which can describe the crustal and upper mantle deformation at different depths.

In recent years, the China Earthquake Network (CEA), the provincial Network, and various scientific research institutes have established numerous broadband seismic stations in this area. These stations provide additional high-quality and continuous observation seismic data. In this study, we apply the direct inversion methods of surface wave dispersion to determine isotropic and azimuth anisotropic shear-wave velocities (Fang et al. 2015; Liu et al. 2019). Our study region spans 21° N to 30° N and 99° E to 106° E (Fig. 1), covering the southern Chuandian and part of the northern Chuandian block.

Data and phase velocity measurements
Data
In this study, we collected the 69 national broad-band permanent stations operated by CEA during 2014–2015 and 22 broad-band seismic stations operated by the Seismic group of Central South University at the interaction of the Xiaojiang fault and Red River fault zone during 2018–2020. At the same time, we have also selected 2-years continuous waveform data of 50 broadband temporary seismic stations in the southern Xiaojiang fault zone during 2008–2010, which were operated by the China Earthquake Administration supported by the project "Quantitative Study on the Medium and Long term Seismic Potential of the Xiaojiang Fracture zone". We have 141 broad-band seismic stations that can provide high-quality continuous observation data and good coverage for the study area (Fig. 1).

Dispersion curve of Rayleigh wave
We first resampled the original waveform data to 1 Hz and removed the mean, trend, and instrument response for the vertical component waveform data. The data are then filtered in the 5–45 s period band and processed with time domain normalization. Finally, the traces are cross-correlated between all station pairs daily. By assuming an isotropic model at the environmental noise field, we stacked the time-reversed cross-correlation to build a symmetric cross-correlation. Finally, all the available daily cross-correlations were stacked for a given station pair. The details of the principle and data processing process of ambient noise tomography have been introduced in previous studies (Shapiro and Campillo 2004;

Gao *et al. Geoscience Letters*   (2024) 11:40

Page 4 of 19

Yao et al. 2005, 2006; Bensen et al. 2007). Following Yao et al. (2005), the empirical Green's function is expressed as:

$$\frac{dC_{AB}(t)}{dt} = -\widehat{G}_{AB}(t) + \widehat{G}_{BA}(-t) \approx -G_{AB}(t) + G_{BA}(-t), -\infty \le t \le \infty \quad (1)$$

where $C_{AB}(t)$ is the cross-correlation function of station A and B; $G_{AB}(t)$ is the Green function associated with waves propagating from station A to station B; $G_{BA}(-t)$ is the reverse Green function associated with waves propagating from station B to station A; $\widehat{G}_{AB}(t)$ and represent the corresponding empirical Green functions and t represents travel time. Empirical Green functions computed for 69 national stations, 50 temporary stations, and 22 broad-band stations are shown in Fig. 2, respectively. Obvious surface-wave moveouts for both directions after being arranged were shown in these figures based on the distance between station pairs.

The phase velocity dispersion of fundamental mode Rayleigh waves was extracted using time–frequency analysis (Yao et al. 2005). The signal time window is defined by assuming phase velocities between 2.5 and 4.5 km/s (Fig. 3). The noise part is considered the envelope of a 150-s-long window immediately following the signal window. We set the signal-to-noise ratio to 5 and the station spacing to more than 2 times the wavelength to satisfy the time-harmonic expression of surface wave propagation in the far field (Yao et al. 2006). We further selected the phase velocity dispersion based on the following criteria. Rayleigh wave dispersion data were initially picked automatically (Fig. 3a). We adopt the quality control strategy of two-trial-and-error inversion, firstly eliminate the outlier dispersion data with travel time residual more than 5 s, and then eliminate the outlier dispersion data with travel time residual more than 3 times standard error (Fang et al. 2010). We obtained 3377 reliable dispersion curves in the period range of 5–45 s (Fig. 3b). The blue dots represent the average measured phase dispersion curves in Fig. 3b. The number of ray paths of different periods is plotted in Fig. 4. The number of measurement phase velocities gradually increases from ~2500 in the 5–30 s period range to a maximum of ~3000 in the range of 15–20 s. The minimum ratio value of station distance to wavelength will give the maximum period of dispersion analysis, so fewer ray paths may satisfy the conditions at the 45 s period, and the extracted dispersion information is also less (Fig. 4).
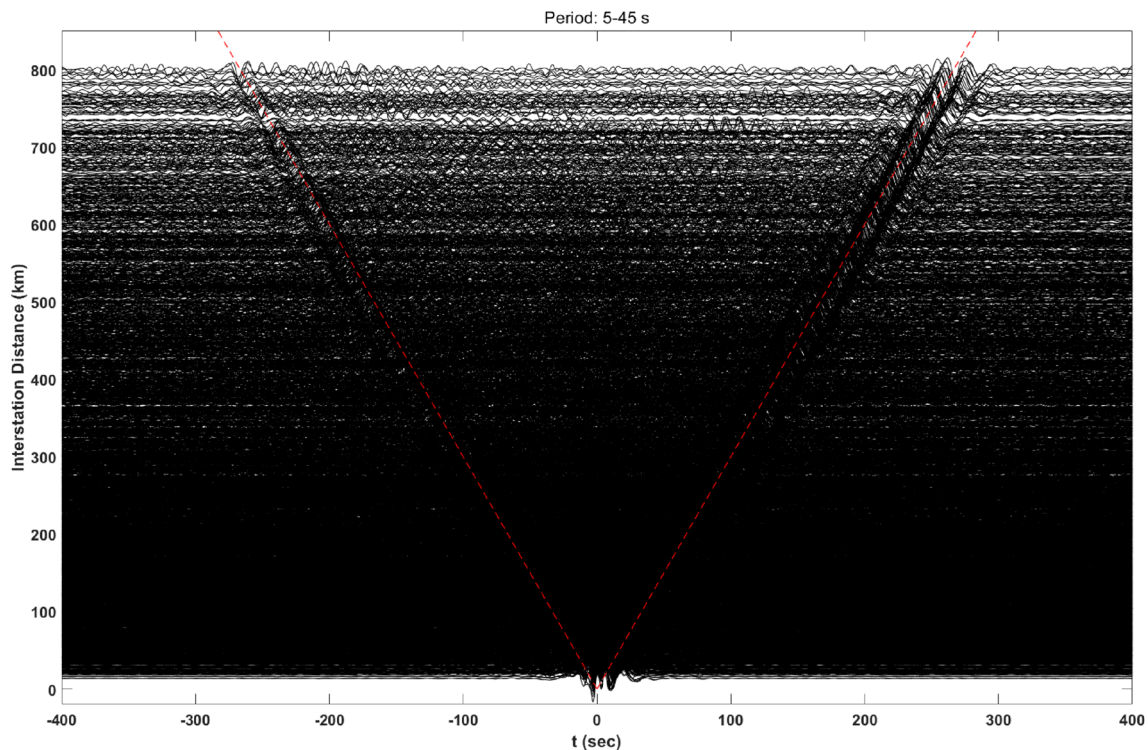

Fig. 2 Cross-correlation of 141 national stations (the red lines refer to the expected arrival times of the surface wave with a group velocity of 3.0 km/s)
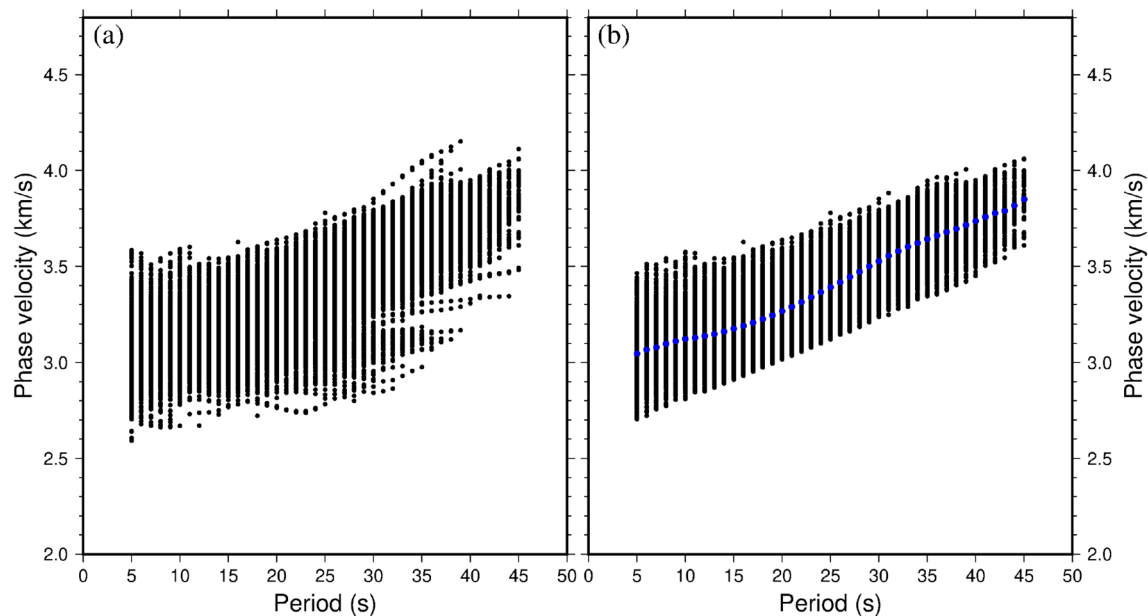
Gao *et al. Geoscience Letters*   (2024) 11:40

Page 5 of 19

Fig. 3 Phase velocity dispersion curves at different periods, **a** automatically picking of the phase velocity dispersion curves, **b** after the removal of outliers, the blue dots represent an average phase velocity of different periods
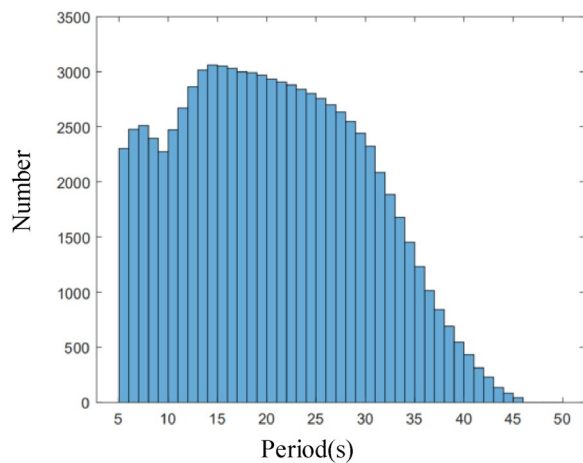

Fig. 4 Number of ray paths in different periods

Direct inversion for 3D shear wave velocity

We applied the direct inversion method (Liu et al. 2019) to calculate the 3-D shear wave velocity and shear wave azimuthal anisotropy. Fang et al. (2015) developed a one-step inversion method, which can directly invert shear wave velocity structure using dispersion data from Rayleigh surface wave with mixed path. This method is based on the fast process method proposed by Rawlinson and Cambridge (2004) for simulating the ray path of surface waves in heterogeneous media. Therefore, the influence of surface wave propagation in complex media in

different periods of non-great circle path is considered in the inversion process, which can effectively improve the inversion accuracy of short-period dispersion data. In the process of inversion of shear wave velocity, based on the empirical formula given by Brocher (2005), P-wave velocity and density were coupled together with shear wave velocity. Liu et al. (2019) added azimuthal information into the slowness expression based on the direct inversion method of surface wave (Smith and Dahlen 1973; Montagner and Nataf 1986), developed a method to obtain a three-dimensional azimuthal anisotropic shear wave velocity model by direct inversion of Rayleigh surface wave mixed path dispersion data. It includes two steps: (1) inverting the 3D isotropic shear wave model based on Rayleigh wave travel time, and (2) joint inversion of the observed 3D isotropic shear wave perturbation and the shear wave azimuthal anisotropy. The joint inversion can enhance the smooth constraints of the inversion results and improve accuracy. In recent years, this method has been extensively utilized for the investigation of velocity structure imaging and azimuthal anisotropy in the southeast margin of the Tibetan Plateau, Sichuan Basin and its adjacent area, and the Tanlu fault zone (Liu et al. 2019; Zhang et al. 2022a, b; Bem et al. 2022), yielding imaging results with a high level of reliability. We first choose the SWChinaCVM-1.0 (Yao 2020; Liu et al. 2021a) as the initial model. The Rayleigh wave travel time related to the frequency was subsequently measured using a grid resolution of $0.5° \times 0.5°$ in both longitude and latitude, based

Gao *et al. Geoscience Letters*   (2024) 11:40

Page 6 of 19

on this model. We opted for a depth discretization of 12 layers with an interval of 5 km.

Results

Checkerboard tests

To check the inversion results obtained by the method and data, we designed a synthetic two-dimensional shear wave velocity model based on conventional checkerboard resolution tests (Rawlinson and Spakman 2016). We first performed a theoretical shear wave velocity model with an anomaly size of 1°×1° in the checkerboard test. We then calculated the theoretical Rayleigh wave travel time based on the ray path of station pairs. The peak velocity perturbation of high- and low velocities are ±5%, respectively. Moreover, 2% random noise was added to the forward model. Figure 5 shows a two-dimensional theoretical shear wave velocity model and the isotropic checkerboard test at different depths. Comparing the input models (Fig. 5a–d) and inversion results (Fig. 5e–h), the isotropic model has a good recovery in both deep and shallow structures in the intersection of the Red River fault and Xiaojiang fault and the south part of the Xiaojiang fault with dense ray paths (Fig. 5). Figure 6 displays the path coverage at four different periods. Meanwhile, due to the sparse distribution of seismic stations

(Fig. 6) in the regional edge, the checkerboard test at four boundaries has a lower resolution than that of the center region.

Based on the isotropic checkboard test, we analyzed the anisotropic checkboard test. The isotropic parameters are kept unchanged in the checkerboard test for azimuthal anisotropy, while only the anisotropic parameters were set as anomalies. The grid spacing is 0.5×0.5°. We set the fast direction of azimuthal anisotropy perpendicular to each other in adjacent abnormal grids and the strength of the azimuthal anisotropy of 2% in the input model (Fig. 7a). 0.2% random noise was also added to the azimuthal anisotropy model. The recovery results are shown in Fig. 7b–f. We found that the recovery inversion results in the dense station areas are well recovered with good coverage of the ray path, such as the south part of the Xiaojiang fault, the interaction of the Red River fault and Xiaojiang fault, and the center of the study area. The fast directions of the azimuthal anisotropy model are well recovered. However, due to the sparsity of ray paths in the northwest and four regional edges, the resolution of the checkboard test is not as good as in the center study area. The angles of the fast directions observed from the retrieved results are consistent with the original model. Although the amplitudes of azimuthal anisotropy are not
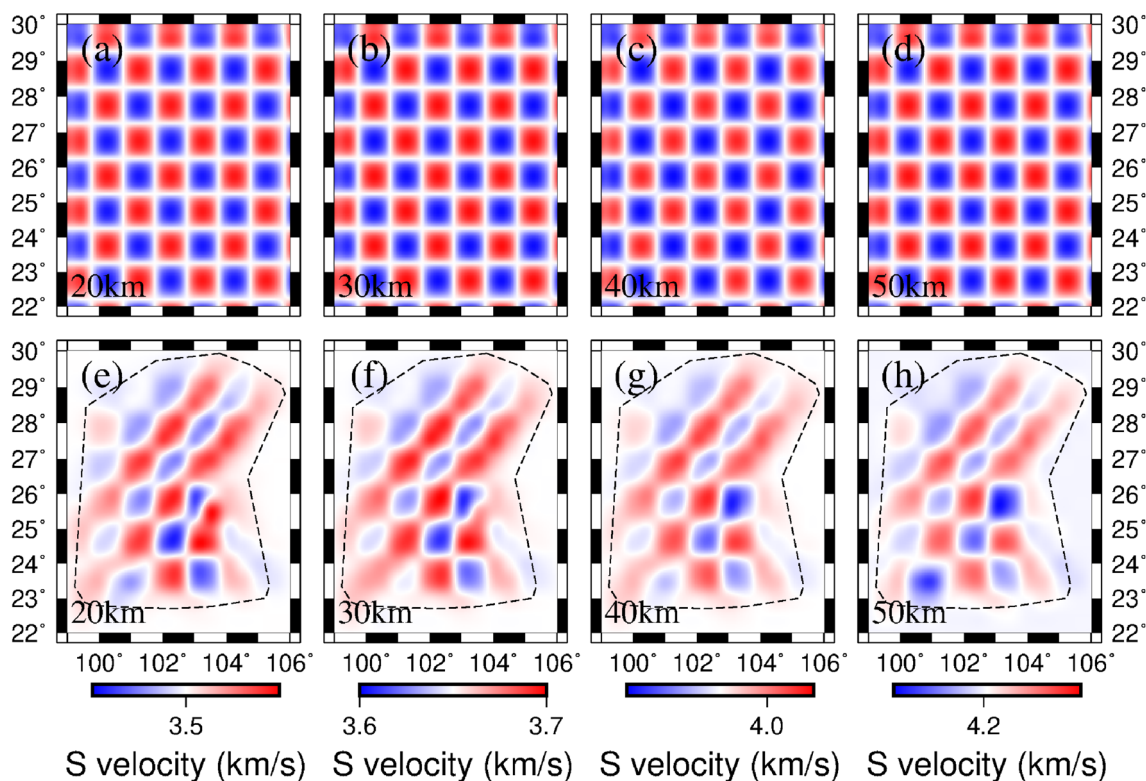

Fig. 5 Checkerboard test for Surface wave isotropic structure. **a**–**d** are the input mode, **e**–**h** are the inversion results at a depth of 20, 30, 40 and 50 km
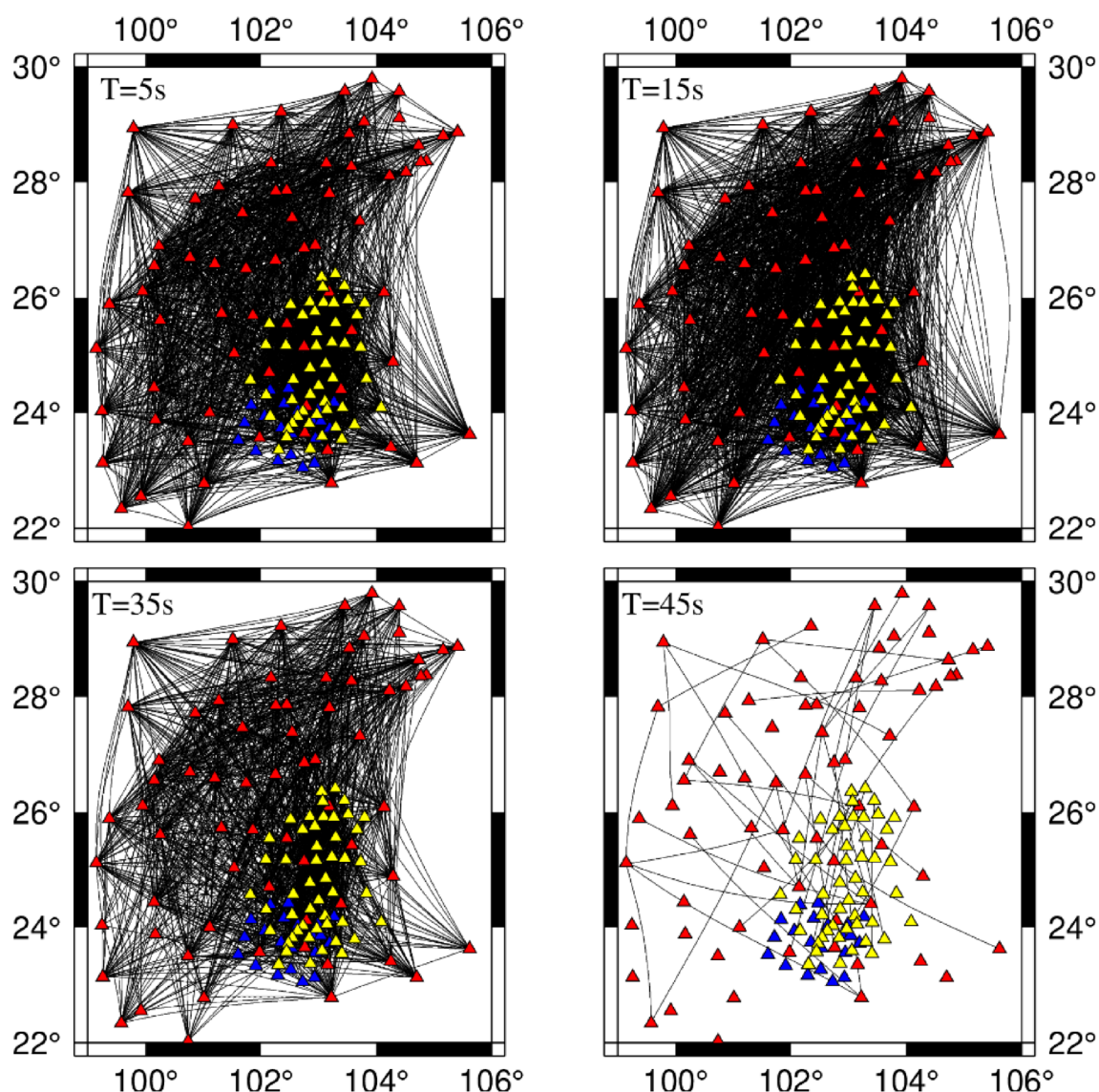
Fig. 6 The ray path at the period of 5 s, 25 s, 35 s, and 45 s (the triangles represent the stations, and the black lines refer to the ray paths)

recovered sufficiently, the fast wave directions obtained from inversion are relatively stable. Therefore, we mainly analyze and discuss the fast direction in subsequent inversion results.

3D shear wave velocity

The inverted isotropic S wave velocities at the depths of 10, 20, 30, 40, and 50 km are shown in Fig. 8. Four vertical images along the lines of Fig. 9 are shown in Fig. 10. Significant low-velocity anomalies are widely observed around the fault zones (Red River fault and Xiaojiang fault) above 10 km and the shallow sedimentary layer in the Sichuan Basin (Fig. 8a and 8b). In comparison, high-speed anomalies are distributed in the Sichuan

Basin. Two ranges of low-velocity anomalies are found along the significant strike-slip faults in the depth range of 20–40 km, which are similar to the results of previous studies in the periods of 15–35 s (Wang et al. 2015; Han et al. 2017; Wu et al. 2019; Liu et al. 2019). The west low-velocity range is mainly concentrated in the Lijiang–Xiaojinhe fault and rotates to the SE direction along the Red River fault with a low-velocity value of 3.3 km/s. In contrast, the east range extends along the Xiaojiang fault from the northern part of the Chuandian block. A columnar high-speed anomaly is enveloped in the middle of the southern Chuandian block by low-velocity anomalies on both the east and west sides. This high-velocity anomaly is located around the
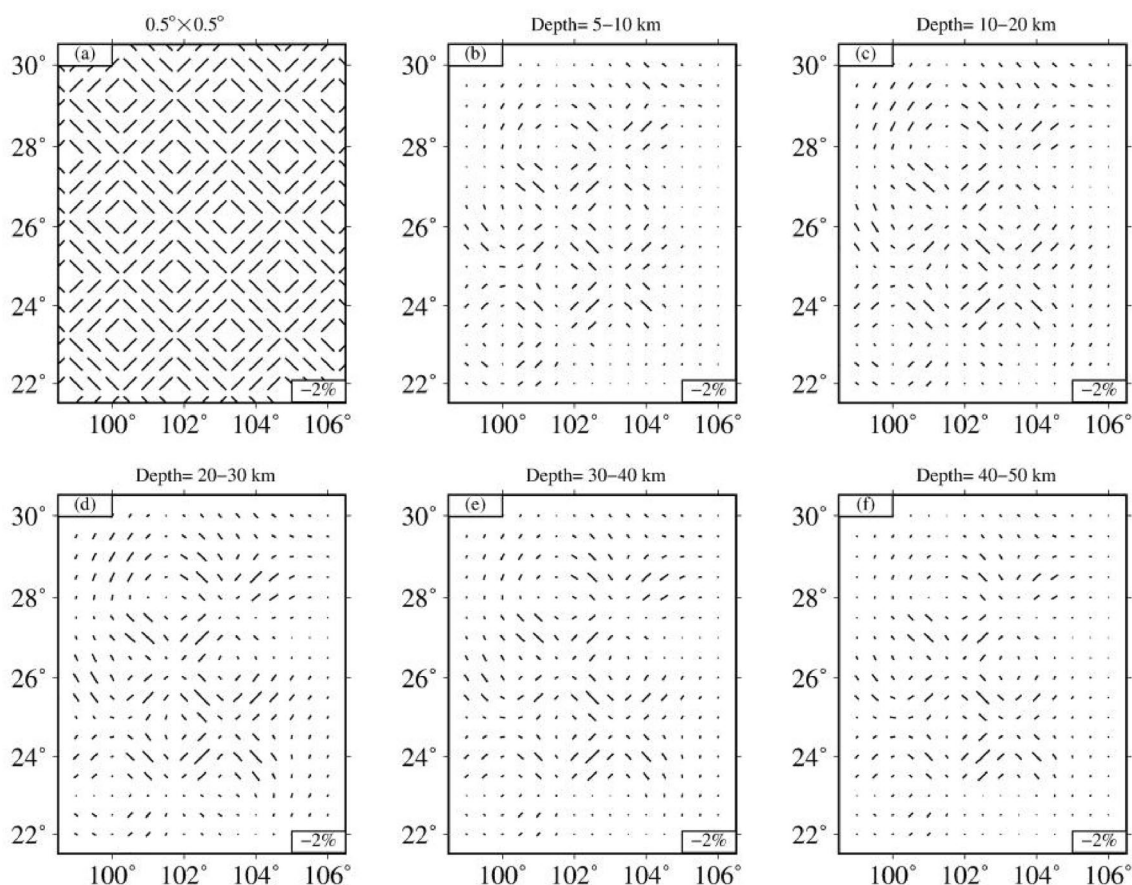
Gao *et al. Geoscience Letters*   (2024) 11:40

Page 8 of 19

Fig. 7 Checkerboard test for azimuthal anisotropy. **a** is input model, **b**–**f** are the inversion results at different depths

inner Emeishan Large Igneous Provinces (ELIP), similar to the observations of previous studies (Bao et al. 2015; Liu et al. 2019; Zhang et al. 2020). Our results also show that two ranges of low-velocity anomalies converge at 26–27° N and 102–103° E at a depth of 40 km. At 50 km depth, the low-velocity anomalies disappear in the southern Chuandian block, mainly concentrating in the northern part of the Chuandian block, which might be attributed to the different crustal thicknesses between the northern and southern parts of the Chuandian block. Previous Rayleigh wave and Love wave tomography studies have also identified the low-velocity anomaly only in the north Chuandian block in the depth range of 45–60 km (Wu et al. 2019; Han et al. 2017; Zhang et al. 2020). Receiver function results (Sun et al. 2012; Wang and Gao 2014; Wang et al. 2017) showed that the crustal thickness in the southern part of the Chuandian block is about 40 km, while it reaches to ~ 60 km in the northern Chuandian block (Sun et al. 2012; Li et al. 2017), indicating that observed low-speed anomalies in the Yunnan area only exit in the crust.

The earthquake events that have occurred in the past 22 years are also depicted (Figs. 9, 10). It is evident that seismic activity predominantly transpired along the Xiaojiang Fault, the northern segment of the Red River fault, and the Lijiang–Xiaojinhe fault zone, indicating these fault zones as seismogenic environments. The frequency of major earthquakes (> Ms 5.5) in the southern section of the Red River fault (elliptical region in Fig. 9) is comparatively lower than that in other deep and major fault areas within Yunnan Province. There have been a few major earthquakes in the south section over the past several hundred years (Shi et al. 2018; Trinh et al. 2012).

The shear wave velocity profile AA' (Fig. 10) across the Chuandian block and the western Yangtze block shows two distinct low-velocity zones in the 20–40 km depth range. Two low-velocity anomalies are separated by a high-speed anomaly in the center of the Chuandian block. The Moho interface (marked by the black line in Fig. 10) gradually decreases from 50 to 35 km from west to east, consistent with the previous studies (Sun et al. 2012; Yang et al. 2010). It suggests that the crustal thickness in the Chuandian block is relatively thicker than
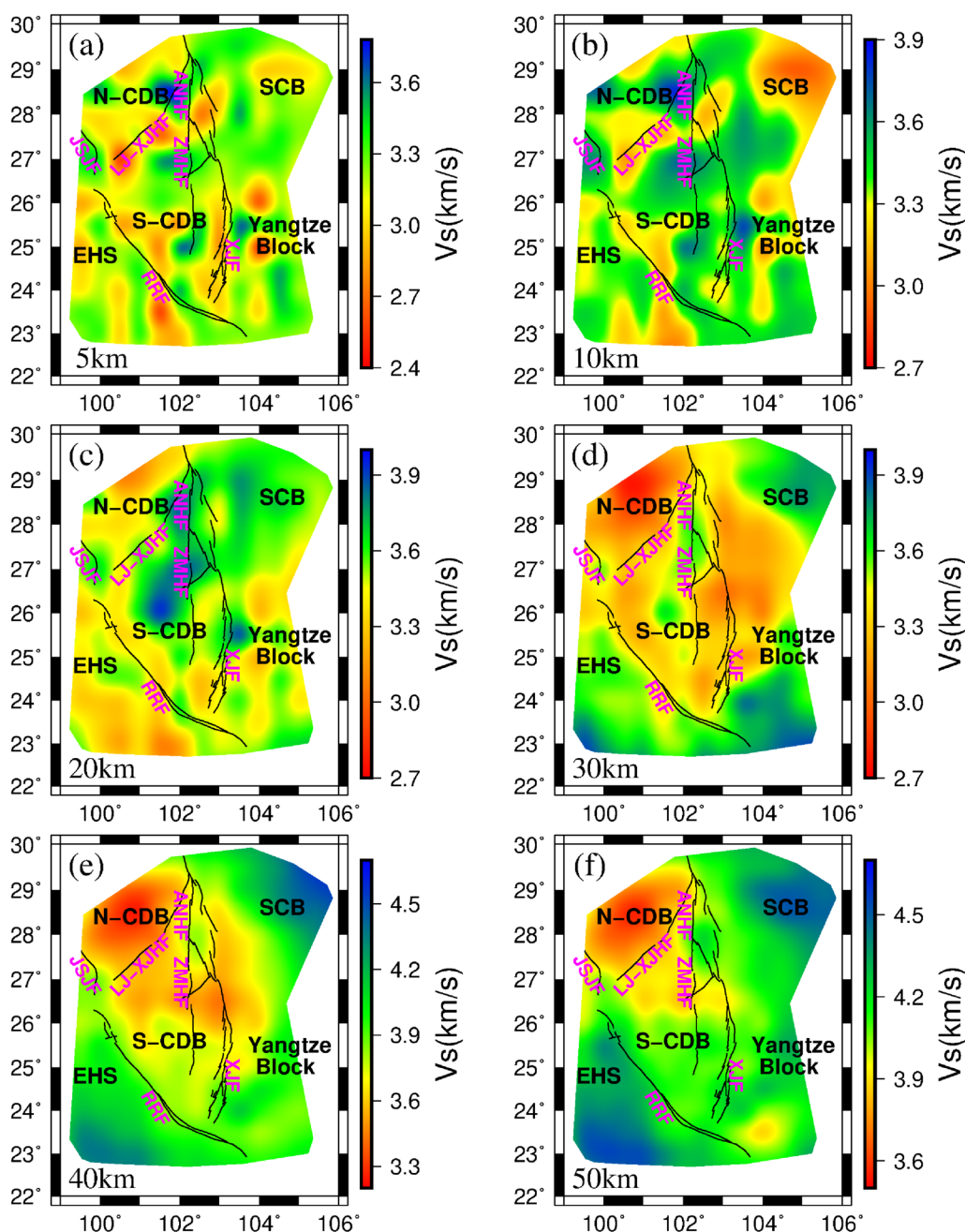
Fig. 8 Isotropic shear wave velocity images at 10, 20, 30, 40, and 50 km depth (**a–f**), black lines represent the major faults

that of the Yangtze block. Profile BB' shows a continuous low-speed anomalous of ~3.3 km/s widely spread above the crust-mantle boundary, which extends from the Eastern Himalayan Syntaxis to the Xiaojiang fault. The Moho surface varies gently in the southern and eastern parts of Yunnan, with crustal thicknesses of 40 km (Fig. 10), consistent with the results of Ling et al. (2020). The profile CC' shows the low-speed anomalies in the 20–40 km depth range beneath the northern Chuandian block, the

Xiaojiang fault and its east side. However, there are relatively high-speed anomalies in the interaction of the Lijiang–Xiaojinhe fault and the Xiaojiang fault above 20 km. The topography of the Moho interface varies from 55 km at 100°–102° E to 45 km at 102.5°E, and then gently with crustal thicknesses of 45 km in the west–southwest of Xiaojang fault. Profile DD' shows that the crustal thickness of the southwestern Red River fault is relatively thinner than that of the center of the Chuandian block
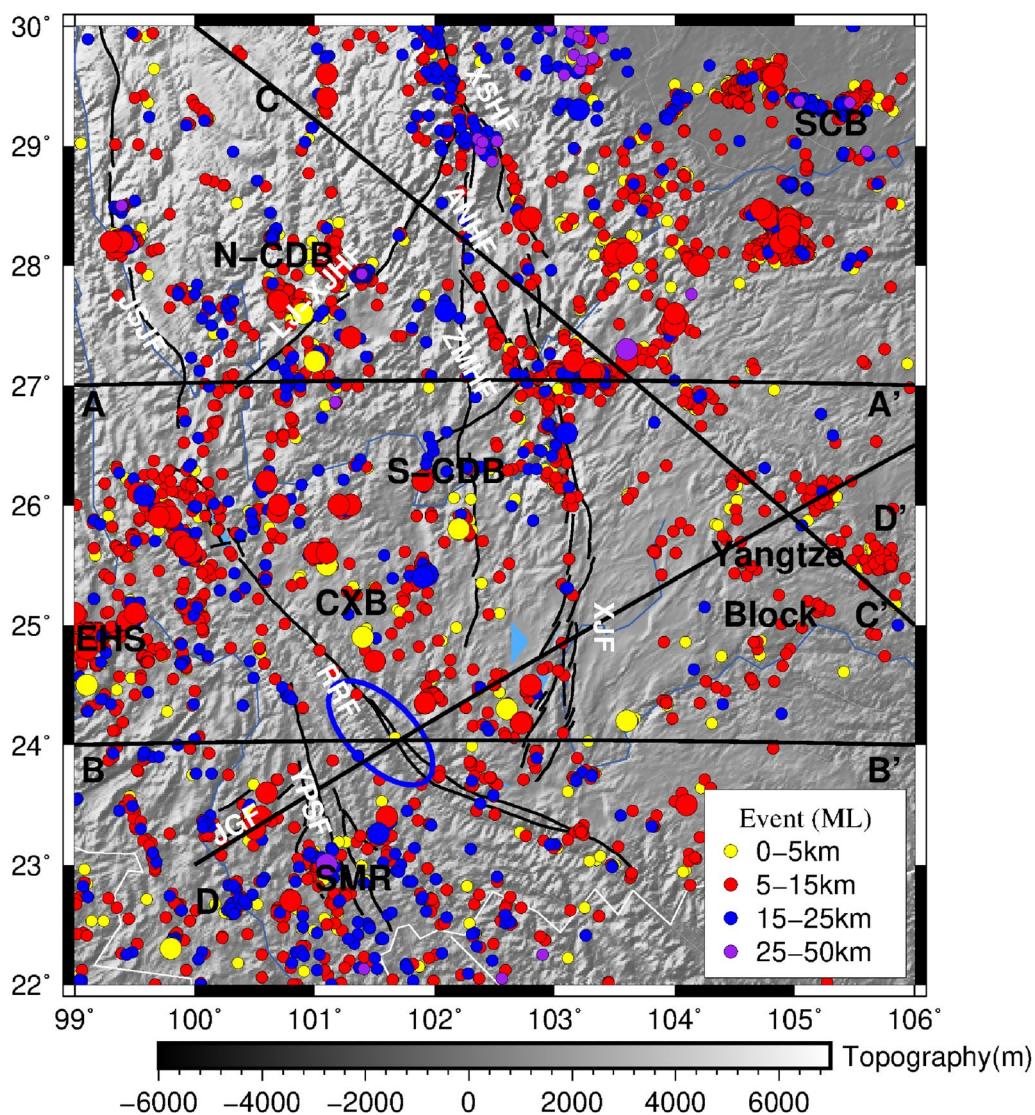
Fig. 9 Distribution of seismic events from 1999 to 2021 and the black straight lines denote the location of vertical profiles. The yellow circles represent the magnitude of Ms 2–5 seismic events, the red circles represent the seismic events with a magnitude larger than 5, and the blue elliptical area is the predicted Red River seismic gap

and the western Yangtze Craton. The distribution of earthquakes in the four vertical profiles indicates that earthquakes mainly occur in the boundary of high- and low-velocity, especially near the large and deep fault zones. The earthquakes might relate to the velocity transition zone and the deformation of the large-scale fault zone.

Shear wave azimuthal anisotropy

We further calculate the shear wave azimuthal anisotropy at different depths in Fig. 11, which also indicates two prominent low-speed zones around the large deep faults (Fig. 11b–d). These two branches of low-velocity zones

are consistent with the isotropic results. The low-speed anomaly gradually becomes confined to the north Chuandian block when the depth reaches 50 km (Fig. 11e). The fast direction of observed shear wave azimuthal anisotropy is approximately N–S in most of our study area in the depth range of 5–20 km, except the southwest margin of the Sichuan Basin (Fig. 11a–c), which is generally consistent with the strike of the tectonic structure and the extension stress. It has a large-scale anti-clockwise in the southwest margin of the Sichuan Basin, consistent with the result of Zhang et al. (2022a, b). Below 25 km (Fig. 11d–f), the fast direction gradually rotates from the N–S in the north part of the Chuandian block to the
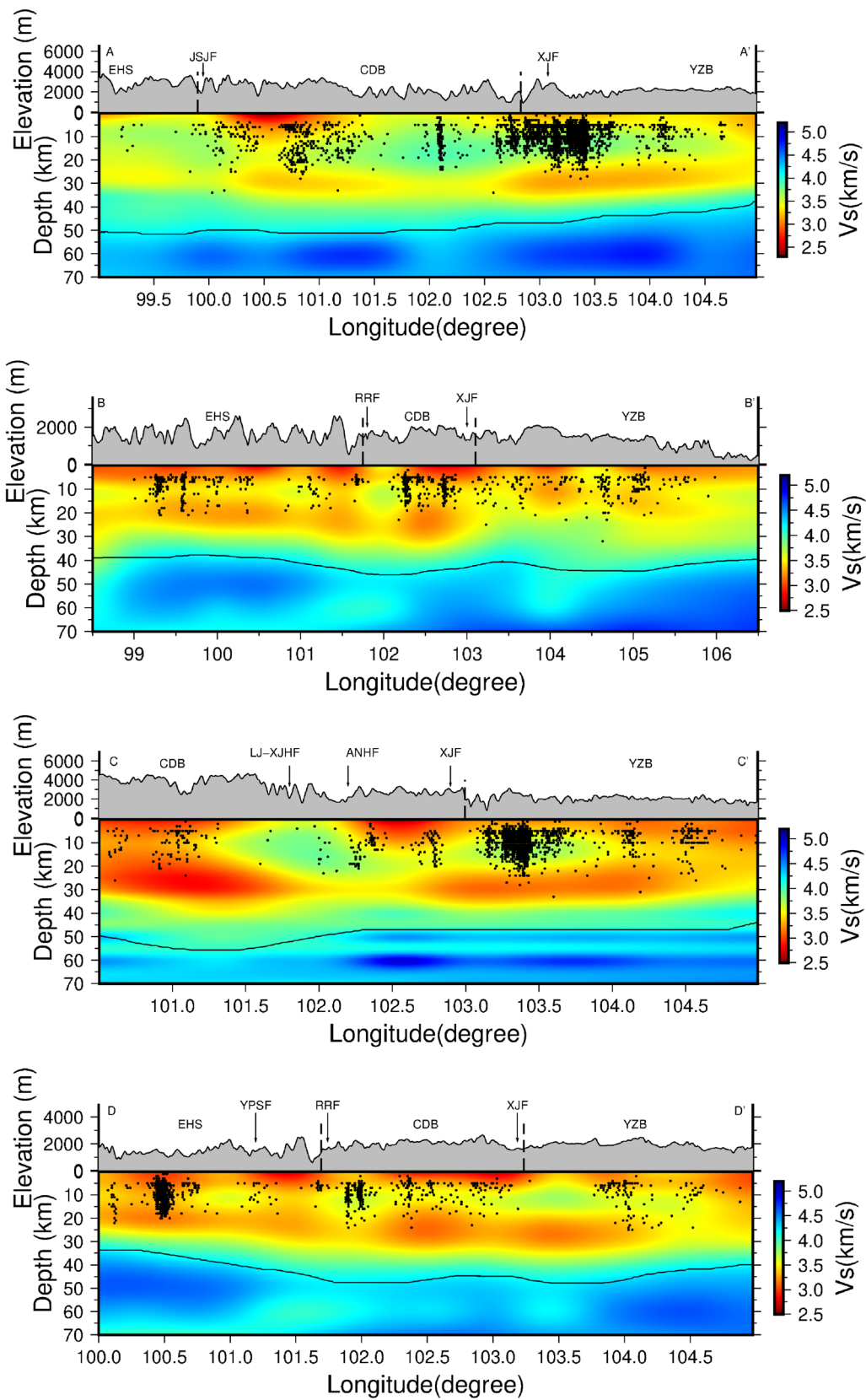
Fig. 10 Vertical profiles of shear wave velocity of the four measuring lines in Fig. 9. Black dots indicate seismic events in the past 22 years within 0.2 degrees near the profile. The black solid lines represent the Moho surface, referring to Sun et al. (2012)
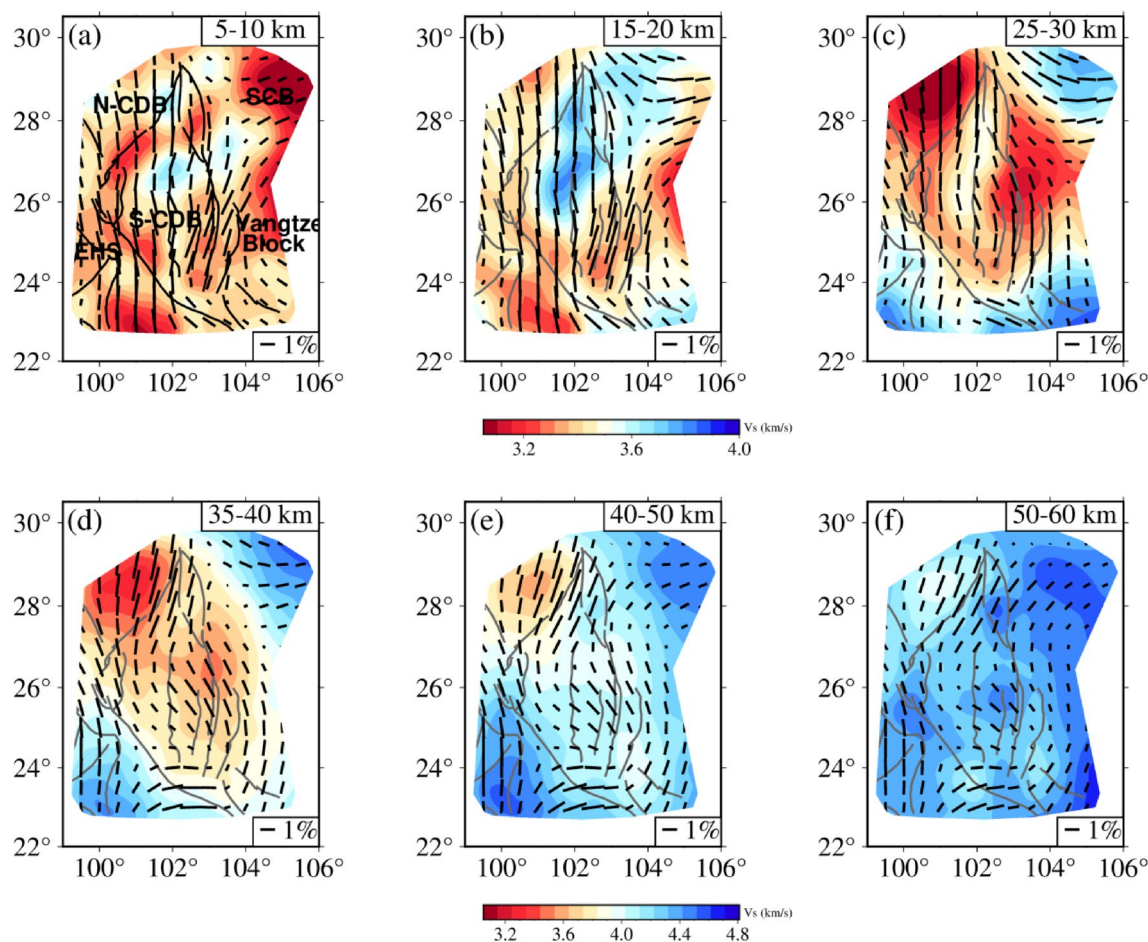
Gao *et al. Geoscience Letters* (2024) 11:40

Page 12 of 19

Fig. 11 Lateral slices of 3-D shear wave azimuthal anisotropic velocity, (**a–f**) denote the depths range of 5–10, 15–20, 25–30, 35–40, 40–50, and 50–60 km, respectively

NE–SW along the Lijiang–Xiaojinhe fault and has an anti-clockwise around the inner core of Emeishan Large Igneous Provinces. It transforms clockwise in the southern Xiaojiang fault and the west Yangtze Craton, which is different from the previous results that show the fast direction is N–S and parallel to the strike of the Xiaojiang fault (Wang et al. 2015; Wu et al. 2019). The fast direction is generally similar to the extension of the low-speed anomaly.

To more clearly demonstrate the variation in the direction of anisotropic fast waves at vertical depth, we have also drawn two vertical profiles with anisotropic distributions (Fig. 12). The fast direction rotates from the N–S direction in the shallow part (above 20 km) to the near E–W direction in the deep part (below 35 km) around the interaction of the Xiaojiang-Red River faults zone (Fig. 11d, Fig. 12 BB'), which agrees with the result of Wu et al. (2019) and Yao et al. (2010). The strength of azimuthal anisotropy in the south part of the Red River fault zone (blue elliptical area in Fig. 9) and the southwest

Sichuan basin gradually extends to the southeast and deeper depths (Figs. 11, 12). The fast direction of azimuthal anisotropy has shifted from approximately N–S to E–W at the intersection of the Red River and Xiaojiang fault zones near 25° N (Figs. 11, 12).

Discussion
Comparison with previous results
The measured tomographic result displays some features similar to previous surface tomography results (Yao et al. 2008; Bao et al. 2015; Wang and Gao 2014; Wang et al. 2015; Han et al. 2017; Liu et al. 2019; Qiao et al. 2018; Zhang et al. 2020). For example, two apparent low-speed anomaly belts are observed along the large deep faults in the lower crust. In contrast, prominent high-speed anomalies are revealed above 25 km with a northeast direction from the center Emeishan area to the southwest Sichuan basin, which separates two large low-speed anomalies (Figs. 8, 10, 11a–d). Meanwhile, the measured fast polarization axes of azimuthal anisotropy
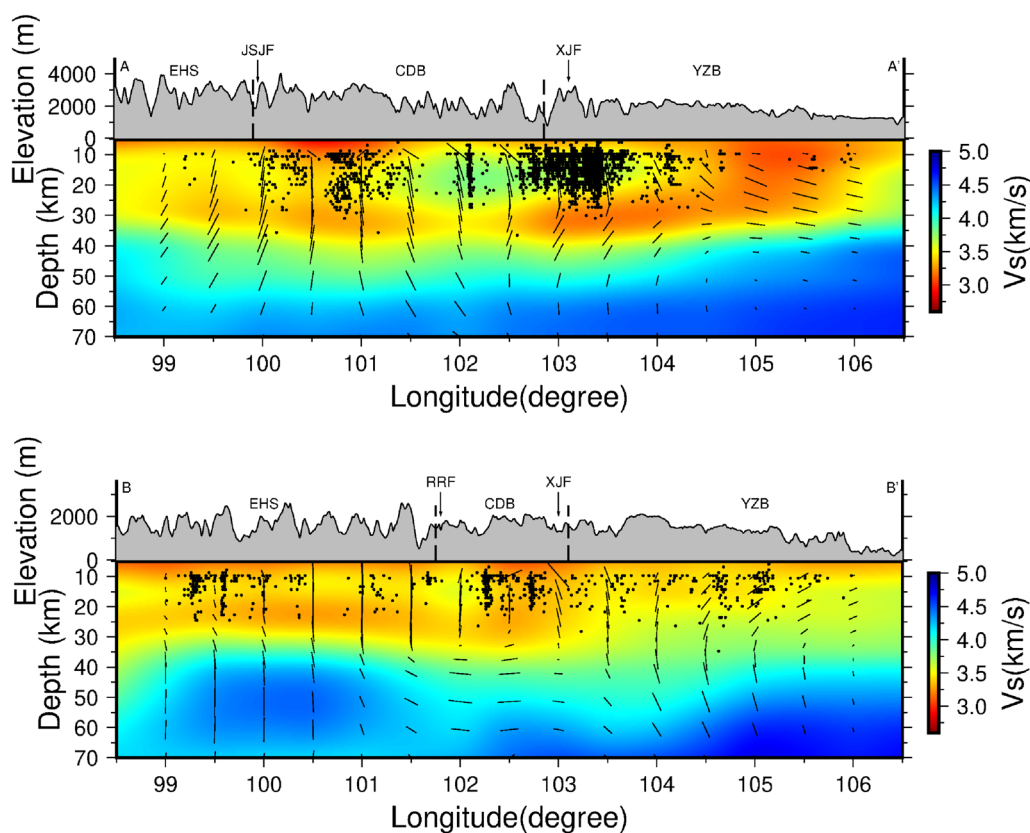
Fig. 12 Vertical profiles of shear wave and azimuth anisotropy of the two measuring lines in Fig. 9 (profile AA', BB'). Black dots indicate seismic events in the past 22 years within 0.2 degrees near the profile. The abbreviations of blocks and faults are the same as in Fig. 1. The fast axis direction and magnitude of anisotropy in a geographic map view are represented by short black lines. The vertical bar and the horizontal bar in the profiles indicate the azimuthal anisotropy's fast direction with N–S and E–W, respectively

also have similar characteristics to the previous results that are subparallel to the large deep strikes of low-speed anomaly belts, such as Xiaojiang fault, Lijiang-Xiaojinhe fault (Liu et al. 2019; Chen et al. 2016; Han et al. 2022). However, our results also reveal some new features. Wu et al. (2019) showed that the west zone of low velocity does not flow along the Red River fault but extends to the southwest direction through the Red River fault zone. Zhang et al. (2020) displayed that the east low-speed anomaly is separated from the north Chuandian block by the high-speed that extends from the inner Emeishan to the southeast Sichuan basin. They deduced that the low-velocity zone beneath the Xiaojiang fault may relate to the crustal thickening after the plateau uplift in this area, which increases crustal temperature, high-temperature melting (Wang and Gao 2014; Zhang et al. 2020). Whereas our result shows that the west low-velocity zone rotates from the Lijiang-Xiaojinhe fault to the Red River fault and extends to the southeast direction along the Red River fault, and the east low-velocity zone is connected to that of the north Chuandian block in the depth range of 25–45 km. Our result also shows that the

two low-velocity anomalies are merged at the intersection of the Xiaojiang fault and the Red River fault in the 25–40 km depth range. The converging low-speed anomaly turns to the southeast, mainly concentrates in the southern section of the Xiaojiang fault zone, and extends southward along the Xiaojiang fault zone in the depth range of 35–40 km. Meanwhile, there is strong anisotropy in the low-speed anomaly, with the fast wave direction extending along the low-speed anomalous body.

On the other hand, due to the sparse station distribution, Liu et al. (2019) displayed insignificant azimuthal anisotropy in the northern low velocity of the Xiaojiang fault. Wu et al. (2019) showed that the fast directions in the west low-speed anomaly around the north of Red River fault are nearly W–E in the 10 and 20 s periods of Rayleigh wave phase-velocity, while this study shows that the fast direction rotates to NW–SE along the Red River fault in the 15 s period. Our model clearly shows significant anisotropy in the low-velocity north of the Xiaojiang fault with the fast direction aligned well with this strike-slip fault orientation. The fast directions rotate from the N–S direction in the lower crust to the NW–SE along

the extension of the low-speed anomaly in the Red River fault zone and then turn to the E–W in the 40–60 km depth range at the intersection of the Xiaojiang fault and Red River fault. The fast directions are consistent with the orientations of the main faults, such as the Lijiang-Xiaojinhe fault and the Red River fault. Similar features are also observed in the 3D seismic azimuthal anisotropy image at the same depth by Ai et al. (2023). Moreover, our results suggest that the fast polarizations rotate to the NW–SE along the west margin of the Sichuan Basin.

Shear wave low-velocity anomalies and crustal structure

In the shallow depth of 0–20 km, the middle Chuandian block and the east of Xiaojiang fault are covered with a relatively high-speed anomaly, and the low-speed bodies are mainly distributed along the Lijiang-Xiaojinhe, Xiaojiang and Red River faults (Figs. 10, 11, 12). The seismic events are primarily concentrated beneath deep faults that exceed a depth of 20 km, based on the distribution pattern of earthquakes (Figs. 9, 10, 12). Those indicate that these low-velocity anomalies might relate to the brittle fracture and shear heating near the fault. The brittle deformation has extended to a depth of about 20 km in the upper crust. GPS data showed that the movement and deformation in the upper crust in SE Tibet may be attributed to the shear stress of the large strike-slip faults (Zhang et al. 2022a, b). Therefore, our results support the rigid block extrusion model proposed by previous studies (Tapponnier et al. 2001; Qiao et al. 2018), which suggests that the upper crustal deformation follows large and deep faults.

In the depth range of 25–45 km, two low-speed branches extend southward along the Xiaojiang fault from the Zemuhe fault and southward along the Red River fault zone from the northern part of the Chuandian block and Lijiang-Xiaojinhe fault zone, respectively (Fig. 8). In addition, the low-velocity belts are ductile in an east–west direction and appear to be connected at a depth of about 30 km (Fig. 10). A liner Magnetotelluric sounding also reported a horizontally extensive resistivity layer in the lower crust (Bai et al. 2010; Li et al. 2019a, b, 2020). Seismic wave inversion shows that the low-speed anomalies in the crust on the west side might be caused by the southeastward extrusion from the central Tibetan Plateau (Zhang et al. 2020). Combined low-velocity materials in the lower crust (Ling et al. 2020), and high Vp/Vs ratio (Sun et al. 2012) and high heat flow of ∼ 90 mW/m^2 in the Chuandian block (Hu et al. 2000), previous studies have mostly believed that the low-speed anomalies originated from lower crustal flow during the eastward growth of the Tibetan Plateau associated with the continuous subduction of Indian Plate (Chen and Gerya 2016).

However, the connectivity between the two low-velocity bodies and the direction of lower crustal flow in the south Chuandian block is still unclear due to limited seismic stations. In this paper, we added 22 new broadband seismic stations around the interaction zone of the Xiaojiang–Red River faults and 50 temporary broadband stations around the southern Xiaojiang fault zone, which provide good coverage for surface wave inversion. The topographic reliefs near the Xiaojiang fault, Lijiang–Xiaojinhe fault, and Red River fault are relatively steep in the AA' and DD' profiles in Fig. 10. The profile BB' shows that the terrain is also relatively steep around the west Yangzte Craton with a thick crust (Fig. 10). Geological data confirmed that if the weak low-speed zone materials in the lower crust are blocked by the rigid high-speed body, it will show a relatively steep topographic relief on the surface. Otherwise, it will be a relatively gentle topographic relief (Clark and Royden 2000). Therefore, we believe that the low-speed zone along the Xiaojiang fault zone in the east and the low-speed zone along the Lijiang–Xiaojinhe fault and Red River fault in the west might be attributed to the lower crustal flow associated with the eastward compression of the uplift Tibet Plateau.

The inversion results also show that two ranges of the low-speed anomaly are separated by a relatively high-speed body in the middle and lower crust around the inner belt of Emeishan Large Igneous Provinces. The measured high-velocity body inclines to the northeast and extends from 10 to 30 km in the AA' profile (Fig. 10), corresponding to the inner-middle belt of Emeishan Large Igneous Provinces from Fig. 8. The radial anisotropy shows a strong negative radial anisotropy in the columnar high-velocity body (Fu et al. 2018), which implies that the lattice arrangement of materials in the crust of the inner zone is likely to have experienced vertical migration. The observed residual gravity anomaly (Deng et al. 2014) and high Vp/Vs (Sun et al. 2012) are gradually decreasing from the inner zone of Emeishan Large Igneous Provinces to its middle zone. Combined with the previous studies (Mooney et al. 2012; Liu et al. 2021b; Zhou et al. 2020), we consider that this observed high-velocity body might be attributed to the basic ultrabasic materials during the formation of Emeishan Large Igneous Provinces caused by the mantle plume. When the mantle plume reached the boundary of the Moho surface, it heated the materials of the uppermost mantle and buoyant magma, which squeezed into the lower crust and caused the mafic crust after its cooling (Zhao et al. 2013). Those underplating mafic/ultramafic materials would result in high seismic velocity, high crustal Vp/Vs, and thickened crust in this region. In addition, large lead–zinc ores are widely spread around the observed high-velocity anomaly, which is related to magmatic

Gao *et al. Geoscience Letters* (2024) 11:40

Page 15 of 19

activity in Emeishan Large Igneous Provinces (Liu et al. 2021b). It also confirmed the reliability of the observed high-speed body and its relationship with the magmatic activity in Emeishan Large Igneous Provinces.

The observed high-velocity anomaly extends northeast with its main part in the inner belt of Emeishan Large Igneous Provinces, implying that the mantle plume head is probably located in the inner belt of Emeishan Large Igneous Provinces. We then deduce that these observed low-velocity anomalies in the lower crust are mainly derived from the southeast-ward extrusion of the Tibetan Plateau and blocked by the rigid Sichuan block and the Emeishan Large Igneous Provinces, which was separated into two parts. The east part extends from the Zemuhe fault to the Xiaojiang fault, and the west part rotates to the Lijiang–Xiaojinhe fault and the Red River fault around the margin of the Emeishan Large Igneous Provinces. Due to the regional stress field and the shear strike-slip stress of the Red River and Xiaojiang faults, two ranges of low-velocity anomalies may migrate southward and merge around the south of the inner belt Emeishan Large Igneous Provinces.

With the increase in depth, the low-speed anomalies are restricted to the northwestern Chuandian block at a depth of 50 km (Fig. 11e). It might be controlled by the crustal thickness. The crustal thickness observed from receiver function in the northern Chuandian region is about 50–65 km, while it reduces to ~ 45 km in the south Chuandian block (Wang and Gao 2014; Wang et al. 2018). Therefore, the northern Chuandian block is still located in the lower crust at a depth of 50 km. In contrast, the southern Chuandian block might reflect the shear wave velocity of the upper mantle. Then, at 50 km, the low velocity is reduced in the south Chuandian block, indicating that the crustal flow mainly concentrates in the lower crust.

Azimuthal anisotropy and Crustal deformation

The azimuthal anisotropy can be used to interpret the deformation process and its dynamic mechanisms in this study area. The velocity variation of the azimuthal anisotropic shear wave, as depicted in Fig. 11, exhibits consistency with the isotropic velocity structure within the range of 5–30 km. Furthermore, the orientation of its anisotropic fast wave aligns with previous research findings (Liu et al. 2021a). The accuracy of azimuth anisotropy results is influenced by the coverage of ray path data. By incorporating broadband seismic station data and the temporary seismic stations into our study in the Xiaojiang–Red River fault zone, we can present more detailed information on azimuth anisotropy and crustal structure, particularly regarding the southern section of the Xiaojiang fault and its interaction with the Red River

fault (Fig. 11). The measured azimuthal anisotropy of the upper crust in the South Chuandian block exhibits fast axes that align with the direction of the principal stress in the stable block. This alignment reflects the orientation of fractures induced by stress within the stable block, as depicted in Fig. 11a (Shi et al. 2006; Tian et al. 2019). The fast direction near the fault zone is consistent with the orientations of local strike-slip faults, indicating a strong influence of fault activity on fracture arrangement in these areas (Cai et al. 2016; Zhao et al. 2013). The consistency between fast directions and orientation of local strike-slip faults supports the idea that the deformation of the upper crust is mainly controlled by large strike-slip faults (Fig. 13a). The GPS vectors were further compared with the observed fast direction at 5–10 km and 20–40 km (Fig. 13), revealing that the maximum deviation angle between GPS and the fast direction of upper crustal anisotropy is less than 45 degrees. For the lower crust, the fast direction of azimuthal anisotropy exhibits significant deviation with GPS vectors, particularly at the junction of the Xiaojiang and Red River fault zones. The observed counterclockwise rotation of the fast direction along the Lijiang–Xiaojinhe fault in the north Chuandian block, below 35 km, is consistent with the distribution pattern of the low-velocity anomaly. We further observe that the fast directions above 20 km and below 20 km exhibit disparities. The comparisons of azimuthal anisotropy at different depths, along with GPS data, suggest incoherent deformation mechanisms between the upper and lower crust.

In the 20–40 km depth range, the azimuth anisotropy is consistent with the extension direction of the two low-velocity belts, the fast direction rotates from N–S in the north part of the Chuandian block to NE–SW around the inner Emeishan Large Igneous Provinces and then to the NW–SE in the south Xiaojiang fault. The SKS splitting, which serves as an indicator of deformation in the mantle lithosphere, reveals a predominant fast direction oriented approximately E–W at around 26–22° N (Einat et al. 2006). It shows that the measured azimuthal anisotropy in the lower crust has an apparent difference with the SKS splitting, which suggests that the deformation of the lower crust and lithospheric mantle are decoupled in this study area. The joint inversion of crustal Lg attenuation and Bouguer gravity anomalies also reveals a distinct zone of lower crust characterized by reduced seismic velocities, which is closely associated with major fault systems (Zhou et al. 2020; Liu et al. 2021a). The apparent low-velocity anomalies in the middle and lower crust (Bao et al. 2015; Shapiro et al. 2004; Wang et al. 2015), the high crustal Lg attenuation (Zhao et al. 2013), and the different fast directions of Ps and SKS splitting (Sun et al. 2012; Han et al. 2022) also indicated that the deformation
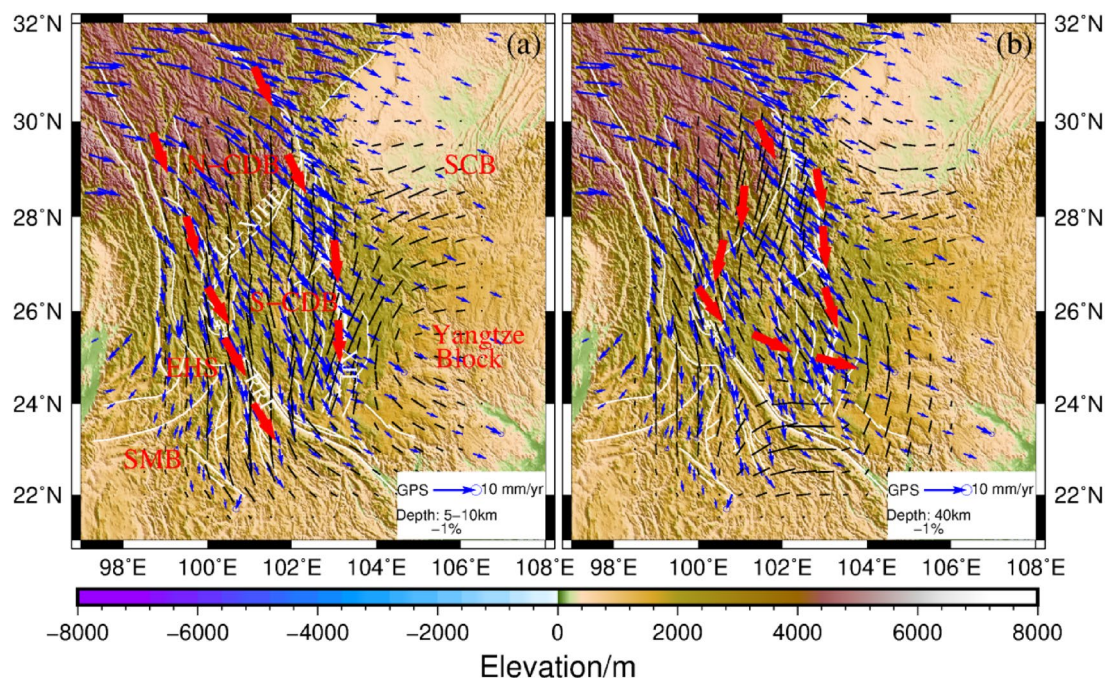
Fig. 13 GPS velocity field from Gan et al. (2007) and Pan et al. (2018) plotted relative to the Eurasia plate (blue arrows) and shear wave azimuthal anisotropy at 5–10 and 40 km (black bar); Red arrows in **a** and **b** inferred the block extrusion and crustal flow, respectively

mechanism is decoupled between the lower crust and lithospheric mantle in most of the south Chuandian block. Combined with the geophysical data and our observations, we deduce that these observed low-velocity anomalies along the significant deep faults in the lower crust might be caused by the lower crustal material flow. The observed shift in the low-speed anomalies trend within the southern Chuandian block also indicates a southeastward rotation of lower crustal flow (Fig. 13b).

Seismic gap

The inversion results show that the west side of the Red River fault is a low-speed zone, while the high-velocity anomaly spreads to the east side, especially in the area above 30 km. The Red River fault, as the southwestern boundary of the southern Chuandian block, is the large and deep fault zone in Yunnan (Zhang et al. 2022a), which is NW trending and managed by a right-lateral strike-slip. It is divided into three sections: north, middle, and south. The distribution of earthquakes in Fig. 9 shows that the major earthquakes (Ms > 5.5) occurred only in the northern part of the Red River fault zone. Although the middle and south segments of the Red River fault are also transition zones of high- and low-velocity anomaly, there is no record of large-magnitude earthquakes in these segments (Yuan et al. 2022). Two possibilities for this case. First, the Red River fault has been sliding in

creep form and only caused the deformation along the fault. Meanwhile, the sliding friction is small, caused by the creep deformation. If the energy does not accumulate along the Red River fault, then the major earthquake has not occurred in the southern part of the Red River fault. Second, the fault is now locked, but the strain has been accumulating along the fault, as the sliding near the fault is not significant. Over time, potential major earthquakes may occur along the fault.

GPS observations showed that the sliding deficit and locking degree of the Red River fault are gradually increasing with time. The strike-slip rates are 4.76 ± 0.78 mm/a, 3.24 ± 0.56 mm/a, and 2.83 ± 0.34 mm/a, with the locking depths, 10.9 km, 11.5 km, and 12.6 km in the north, middle and south part of Red River fault, respectively (Zhang et al. 2022a). GPS observations also showed that the sliding deficit of the south section is 5 mm/a, slightly lower than that of the northern section 9 mm/a (Zhang et al. 2022a). The sliding deficit often reflects the speed of strain accumulation in this area. Therefore, the Red River fault zone has experienced rapid strain accumulation, and the velocity in the north section is faster than in the south section of the Red River fault.

The likelihood of a significant earthquake occurring in the middle and south segments of the Red River fault zone has been extensively examined in numerous studies (Zhang et al. 2022b; Wu et al. 2022; Su et al. 2022). The

Gao *et al. Geoscience Letters* (2024) 11:40

Page 17 of 19

study revealed that seismic activity with high magnitudes in the Red River fault zone has the potential to migrate toward the southwest direction of the Chuxiong–Jianshui fault region (Zhang et al. 2022b). However, the high-resolution remote sensing data and geomorphological surveys (Wu et al. 2022) suggested that several strong seismic activities occurred in the center and south sections of the Red River fault. Additionally, various scales of river system faults have developed along the Red River fault zone (Su et al. 2022). The measured azimuthal anisotropy of the shear wave indicates that the fast direction above 20 km near the Red River fault aligns with the strike-slip fault. However, there are significant differences between the east and west segments of this fault zone (Fig. 11). The fast direction on the western segment of the Red River fault is primarily the N–S direction, while it rotates to NE–SW on its eastern segment. This observation implies that the rates of strike slip and strain accumulation are relatively elevated within the middle-southern segment of the Red River fault zone.

The tectonic stress field in Yunnan revealed that the predominant stress regime is characterized by strike-slip motion, with the maximum principal compressive direction primarily oriented in the northwest-southeast axis (Tian et al. 2019). The azimuth anisotropy of the upper crust of the Chuan-Dian block is roughly aligned with the principal compressive stress direction of the regional tectonic stress field. Moreover, the fast direction of anisotropy in the upper crust near the fault zone is consistent with the strike of the fault zone (Fig. 11), indicating that the upper crust deformation in this region is strongly influenced by strike-slip fault activities (Cai et al. 2016; Zhao et al. 2013). However, the observed fast wave orientations in the northern and central segments of the Red River fault zone exhibit disparities, with indications of deflection in the central section of the Red River fault. The stress state of the Red River fault zone exhibits discontinuity, and the middle section of the Red River fault zone in the middle and upper crust displays a high-velocity anomaly relative to the north section. Electromagnetic inversion shows that there is a high resistance anomaly in that area (Ye et al. 2022). suggesting that the high resistance and high shear wave velocity may lead to stress deflection, potentially resulting in easier stress accumulation within the central section of the Red River fault. In addition, the inversion results of fault strike-slip rate and locking depth indicate that the region is currently in a state of strong tectonic locking (Li et al. 2019a, b). The seismic prediction performance of the Yunnan region was assessed by Wang et al. (2021) based on the *b*-value, revealing a low *b*-value zone located in the central part of the Red River fault, indicating an elevated stress state. Consequently, there exists a heightened seismic risk within this particular section of the Red River fault zone.

Conclusions

We apply the direct joint inversion method to build the 3-D Rayleigh wave velocity and its azimuthal anisotropy at a period of 5–45 s recorded by 141 broadband seismic stations. We mainly get the following three conclusions.

(1) The observed low-velocity anomalies are mainly distributed near the deep and large fault zones in the upper crust, and the fast direction of azimuthal anisotropy aligns well with the strike-slip fault orientations in the upper crust. Based on the depth distribution of seismic events, low-velocity anomalies might relate to the brittle fracture and shear heating near the fault that extends to about 20 km. In the lower crust, two low-velocity branches extend southward along the Xiaojiang fault and the Red River fault zone, respectively. Two low-velocity branches are merged around the junction of Xiaojiang and Red River faults at about 30–40 km. The observed fast direction of significant azimuthal anisotropy in the lower crust mainly follows two major low-velocity anomaly trends, which might be associated with ductile deformation within the lower crust. We deduce two crustal deformation modes in this region. One is the block extrusion model in the upper crust along the deep fault zone, and the other is the two branches of lower crustal flow along the Red River fault and the Xiaojiang fault.

(2) Our result also shows a high-speed body below the inner belt of Emeishan Large Igneous Provinces, while its outer belt shows a relatively low velocity. Combined with geological data and geophysical observations, we infer that the high-speed anomaly might relate to basic ultra-basic materials intruding from the mantle plume into the crust. However, the head of the mantle plume mainly occurs below the inner zone. That is why the two low-speed zones are merged in the south margin of Emeishan Large Igneous Provinces. Those also indicate that the Emeishan igneous rocks in the inner belt of Emeishan Large Igneous Provinces obstructed the low crustal flow and separated into two parts.

(3) We also find that seismic events mainly happen in the boundary of high–low velocity anomalies. However, less large magnitude earthquakes have occurred in the south Red River fault in the past ten years, although this area is the boundary of the high–low velocities zone. Combined with the locking degree and sliding deficit of the south Red River fault zone, we speculate that the south Red River fault zone may be the earthquake gap. However, more evidence needs to be further verified.

Gao *et al. Geoscience Letters*   (2024) 11:40

Page 18 of 19

Supplementary Information

Acknowledgements

Author contributions

Conceptualization, Z.G.; methodology, Z.G. and Q.L.; validation, Z.J. and J.H.;formal analysis, J.H., Z.G., Y. S. and Q.L.; data curation, Y.S. and Z.G.; writing original draft preparation, Z.G.; project administration, Y.S. and J.H. All authors have read and agreed to the published version of the manuscript.

Funding

Availability of data and materials

The datasets used and analyzed during the current study are available from the corresponding author on reasonable request.

Declarations

Competing interests

There are no conflicts of interest concerning the results of this paper.

References

Ai S, Zheng Y, Zeng S, Wang S (2023) Measurements of Rayleigh wave ellipticity anisotropy and implications for distinct crustal deformation styles across the SE Tibet margin. Tectonophysics 856:229863

Bai DH, Unsworth MJ, Meju MA et al (2010) Crustal deformation of the eastern Tibetan plateau revealed by magnetotelluric imaging. Nat Geosci 3:358–362

Bao XW, Sun XX, Xu MJ et al (2015) Two crustal low-velocity channels beneath SE Tibet were revealed by joint inversion of Rayleigh wave dispersion and receiver functions. Earth Planet Sci Lett 415:16–24

Bem TS, Liu C, Yao H, Luo S, Yang Y, Liu B (2022) Azimuthally anisotropic structure in the crust and uppermost mantle in Central East China and its significance to regional deformation around the Tan-Lu Fault Zone. J Geophys Res Solid Earth. https://doi.org/10.1029/2021jb023532

Bensen GD, Ritzwoller MH, Barmin MP, Levshin AL, Lin F, Moschetti MP, Shapiro NM, Yang Y (2007) Processing seismic ambient noise data to obtain reliable broad-band surface wave dispersion measurements. Geophys J Int 169:1239–1260

Brocher TM (2005) Empirical relations between elastic wavespeeds and density in the Earth's crust. Bull Seismol Soc Am 95(6):2081–2092

Cai Y, Wu J, Fang L, Wang W, Yi S (2016) Crustal anisotropy and deformation of the southeastern margin of the Tibetan plateau revealed by Pms splitting. J Asian Earth Sci 121:120–126

Chen L, Gerya TV (2016) The role of lateral lithospheric strength heterogeneities in orogenic plateau growth: insights from 3-D thermo-mechanical modeling.J. Geophys Res 121:3118–3138

Chen H, Zhu L, Su Y (2016) Low-velocity crustal flow and crust–mantle coupling mechanism in Yunnan, SE Tibet, revealed by 3D S-wave velocity and azimuthal anisotropy. Tectonophysics 685:8–20

Chen L, Capitanio FA, Liu L, Gerya TV (2017) Crustal rheology controls on the Tibetan plateau formation during India-Asia convergence. Nat Commun 8(1):15992

Clark MK, Royden LH (2000) Topographic ooze: building the eastern margin of Tibet by the lower crustal flow. Geology 28:703–706

Clark MK, Bush JWM, Royden LH (2005) Dynamic topography produced by lower crustal flow against rheological strength heterogeneities bordering the Tibetan Plateau. Geophys J Int 162:575–590

Deng Y, Zhang Z, Mooney W, Badal J, Fan W, Zhong Q (2014) Mantle origin of the Emeishan large igneous province (South China) from the analysis of residual gravity anomalies. Lithos 204:4–13

Einat L, Maureen DL, Van Der Hilst RD (2006) Seismic anisotropy in Eastern Tibet from shear wave splitting reveals changes in lithospheric deformation Earth Planet. Sci Lett 251:293–304

Fang L, Wu J, Ding Z, Panza GF (2010) High resolution Rayleigh wave group velocity tomography in North China from ambient seismic noise. Geophys J Int 181(2):1171–1182

Fang H, Yao H, Zhang H et al (2015) Direct inversion of surface wave dispersion for three-dimensional shallow crustal structure based on ray tracing: methodology and application. Geophys J Int 201:1251–1263

Fu YV, Jia R, Han F, Chen A (2018) SH wave structure of the crust and upper mantle in the southeastern margin of the Tibetan Plateau from teleseismic Love wave tomography. Phys Earth Planet Inter 279:15–20

Gan WJ, Zhang PZ, Shen ZK, Niu ZJ, Wang M, Wan YG, Zhou DM, Cheng J (2007) Present-day crustal motion within the Tibetan Plateau is inferred from GPS measurements. J Geophys Res 112:B08416. https://doi.org/10.1029/2005JB004120

Han M, Li JY, Xu XY, Hu JF (2017) Analysis for crustal anisotropy beneath the southeastern margin of Tibet by stacking azimuthal receiver functions. Chin J Geophys 60:4537–4556

Han C, Huang Z, Hao S, Wang L, Xu M, Hammond JO (2022) Restricted lithospheric extrusion in the SE Tibetan Plateau: evidence from anisotropic Rayleigh-wave tomography. Earth Planet Sci Lett 598:117837

Hu S, He L, Wang J (2000) Heat flow in the continental area of China: a new data set. Earth Planet Sci Lett 179(2):407–419

Huang H, Yao HJ, van der Hilst RD (2010) Radial anisotropy in the crust of SE Tibet and SW China from ambient noise interferometry. Geophys Res Lett 37:L21310

Lei J, Zhao D, Su Y (2009) Insight into the origin of the Tengchong intraplate volcano and seismotectonics in southwest China from local and teleseismic data. J Geophys Res Solid Earth 114:0148–0227

Li J, Song X, Zhu L, Deng Y (2017) Joint inversion of surface wave dispersions and receiver functions with P velocity constraints: application to Southeastern Tibet. J Geophys Res Solid Earth 122(9):7291–7310

Li DH, Ding ZF, Wu PP, Liang MJ, Wu P, Gu QP, Kang QQ (2019a) Deep structure of the Zhaotong and Lianfeng fault zones in the eastern segment of the Sichuan-Yunnan border and the 2014 Ludian MS65 earthquake. Chin J Geophys 62(12):4571–4587. https://doi.org/10.6038/cjg2019M0450

Li X, Bai D, Ma X, Chen Y, Varentsov IM, Xue G, Xue S, Lozovsky I (2019b) Electrical resistivity structure of the Xiaojiang strike-slip fault system (SW China) and its tectonic implications. J Asian Earth Sci 176:57–67

Li X, Ma X, Chen Y, Xue S, Varentsov IM, Bai D (2020) A plume-modified lithospheric barrier to the southeastward flow of partially molten Tibetan crust inferred from magnetotelluric data. Earth Planet Sci Lett 548:116493

Ling Y, Zheng T, He Y, Hou G (2020) Response of Yunnan crustal structure to eastward growth of the Tibet Plateau and subduction of the India plate in Cenozoic. Tectonophysics 797:228661

Liu C, Yao H, Yang H, Shen W, Fang H, Hu S, Qiao L (2019) Direct inversion for three-dimensional shear wave speed azimuthal anisotropy based on surface-wave ray tracing: methodology and application to Yunnan, southwest China. J Geophys Res Solid Earth 124:11394–11413

Liu Y, Yao H, Zhang H et al (2021a) The community velocity model V.1.0 of Southwest China, constructed from joint body- and surface-wave travel-time tomography. Seismol Res Lett 92:2972–2987

Liu Y, Li L, van Wijk J et al (2021b) Surface-wave tomography of the Emeishan large igneous province (China): Magma storage system, hidden hotspot track, and its impact on the Capitanian mass extinction. Geology 49(9):1032–1037

Montagner JP, Nataf HC (1986) A simple method for inverting the azimuthal anisotropy of surface waves. J Geophys Res Solid Earth 91(B1):511–520

Mooney WD, Ritsema J, Hwang YK (2012) Crustal seismicity and the earthquake catalog maximum moment magnitude (Mcmax) in stable continental regions (SCRs): correlation with the seismic velocity of the lithosphere. Earth Planet Sci Lett 357:78–83

Pan Y, Shen WB, Shum CK, Chen R (2018) Spatially varying surface seasonal oscillations and 3-D crustal deformation of the Tibetan Plateau derived from GPS and GRACE data. Earth Planet Sci Lett 502:12–22

Qiao L, Yao H, Lai Y-C, Huang B-S, Zhang P (2018) Crustal structure of southwest China and northern Vietnam from ambient noise tomography: implication for the large-scale material transport model in SE Tibet. Tectonics 37:1492–1506

Rawlinson N, Sambridge M (2004) Wave front evolution in strongly heterogeneous layered media using the fast marching method. Geophys J Int 156(3):631–647

Rawlinson N, Spakman W (2016) On the use of sensitivity tests in seismic tomography. Geophys J Int 205(2):1221–1243. https://doi.org/10.1093/gji/ggw084

Royden LH, Burchfiel BC, King RW, Wang E, Chen Z, Shen F, Liu Y (1997) Surface deformation and lower crustal flow in Eastern Tibet. Science 276:788–790

Savage MK (1999) Seismic anisotropy and mantle deformation: what have we learned from shear wave splitting? Rev Geophys 37(1):65–106

Schoenbohm LM, Burchfiel BC, Liangzhong C et al (2006) Propagation of surface uplift, lower crustal flow, and Cenozoic tectonics of the southeast margin of the Tibetan Plateau. Geology 34:813–816

Shapiro NM, Campillo M (2004) Emergence of broad-band Rayleigh waves from correlations of the ambient seismic noise. Geophys Res Lett 31:L07614

Shi YT, Gao Y, Wu J, Luo Y, Su YJ (2006) Seismic anisotropy of the crust in Yunnan, China: polarizations of fast shear-waves. Acta Seismol Sin 19:620–632

Shi XH, Sieh K, Weldon R, Zhu CN, Han Y, Yang JW, Robinson SW (2018) Slip rate and rare large prehistoric earthquakes of the Red River fault, Southwestern China. Geochem Geophys Geosys 19:2014–2031

Smith ML, Dahlen FA (1973) The azimuthal dependence of Love and Rayleigh wave propagation in a slightly anisotropic medium. J Geophys Res 78(17):3321–3333

Su Q, Wang X, Yuan D, Zhang H, Lu H, Xie H (2022) Secondary faulting plays a key role in regulating the Cenozoic crustal deformation in the northeastern Qinghai-Tibet Plateau. Terra Nova 34(3):231–243

Sun Y, Niu F, Liu H, Liu JX (2012) Crustal structure and deformation of the SE Tibetan plateau revealed by receiver function data. Earth Planet Sci Lett 349:186–197

Tapponnier P, Peltzer G, Le Dain AY, Armijo R, Cobbold P (1982) Propagating extrusion tectonics in Asia: new insights from simple experiments with plasticine. Geology 10:611–616

Tapponnier P, Xu ZQ, Roger F, Meyer B, Arnaud N, Wittlinger G, Yang JS (2001) Oblique stepwise rise and growth of the Tibet Plateau. Science 294:1671–1677

Tian J, Luo Y, Zhao L (2019) Regional stress field in Yunnan revealed by the focal mechanisms of moderate and small earthquakes. Earth Planet Phys 3(3):243–252

Trinh PT, Liem NV, Huong NV, Vinh HQ, Thom BV, Thao BT, Tan MT, Hoang N (2012) Late Quaternary tectonics and seismotectonics along the Red River fault zone, North Vietnam. Earth-Sci Rev 114:224–235

Wang Q, Gao Y (2014) Rayleigh wave phase velocity tomography and strong earthquake activity on the southeastern front of the Tibetan Plateau. Sci China Earth Sci 57:2532–2542

Wang Q, Gao Y, Shi Y (2015) Rayleigh wave azimuthal anisotropy on the southeastern front of the Tibetan Plateau from seismic ambient noise. Chin J Geophys 58:4068–4078 (**In Chinese with English abstract**)

Wang W, Wu J, Fang L, Lai G, Cai Y (2017) Crustal thickness and Poisson's ratio in southwest China based on data from dense seismic arrays. Geophys Res Solid Earth 122:7219–7235

Wang J, Zhang J, Zhong W, Yang Q, Li F, Zhu Z (2018) Sources of ore-forming fluids from Tianbaoshan and Huize Pb-Zn deposits in Yunnan-Sichuan-Guizhou Region, southwest China: evidence from fluid inclusions and He-Ar isotopes. Earth Sci 43:2076–2099 (**In Chinese with English abstract**)

Wang R, Chang Y, Miao M, Zeng Z, Chen H, Shi H, Li D, Liu L, Su Y, Han P (2021) Assessing earthquake forecast performance based on b value in Yunnan Province, China. Entropy 23(6):730

Wu T, Zhang S, Li M, Qin W, Zhang C (2016) Two crustal flowing channels and volcanic magma migration underneath the SE margin of the Tibetan Plateau as revealed by surface wave tomography. J Asian Earth Sci 132:25–39

Wu T, Zhang S, Li M, Hong M, Hua Y (2019) Complex deformation within the crust and upper mantle beneath SE Tibet revealed by anisotropic Rayleigh wave tomography. Phys Earth Planet Inter 286:165–178

Wu W, Long F, Liang M, Su J, Chen X (2022) Characteristics of stress field and crustal kinematics of the southern region of Sichuan-Yunnan block, southern Tibet Plateau. Quat Int 656:70–79

Xu LL, Rondenay S, Van Der Hilst RD (2007) Structure of the crust beneath the southeastern Tibetan Plateau from teleseismic receiver functions. Phys Phys Earth Planet Inter 165:176–193

Yang Y, Zheng Y, Chen J et al (2010) Rayleigh wave phase velocity maps of Tibet and the surrounding regions from ambient seismic noise tomography. Geochem Geophy Geodesy 11:8

Yang X, Luo Y, Jiang C, Yang Y, Niu F, Li G (2023) Crustal and upper mantle velocity structure of SE Tibet from joint inversion of Rayleigh wave phase velocity and teleseismic body wave data. J Geophys Rese Solid Earth 128:e2022JB026162

Yao H (2020) Building the community velocity model in the Sichuan-Yunnan region, China: strategies and progresses. Sci China Earth Sci 63:1425–1428

Yao H, Xu G, Zhu L, Xiao X (2005) Mantle structure from inter-station Rayleigh wave dispersion and its tectonic implication in Western China and neighboring regions. Phys Earth Planet Inter 148:39–54

Yao H, van der Hilst RD, de Hoop MV (2006) Surface-wave array tomography in SE Tibet from ambient seismic noise and two-station analysis: I - Phase velocity maps. Geophys J Int 166:732–744

Yao H, Beghein C, Van Der Hilst RD (2008) Surface wave array tomography in SE Tibet from ambient seismic noise and two-station analysis-II. Crustal and upper-mantle structure. Geophys J Int 163:205–219

Yao H, Van Der Hilst RD, Montagner JP (2010) Heterogeneity and anisotropy of the lithosphere of SE Tibet from surface wave array tomography. J Geophys Res Solid Earth 115:0148–0227

Ye T, Chen X, Liu Z, Wang P, Dong Z, Cui T, Jiang F, Cai J, Zhang Y, Zhang J, Zhou L (2022) A magnetotelluric study of 3D electrical resistivity structure underneath the southern segment of the Red River fault zone, South China. J Asian Earth Sci 225:105056

Yuan XP, Huppert KL, Braun J, Shen X, Liu-Zeng J, Guerit L, Wolf SG, Zhang JF, Jolivet M (2022) Propagating uplift controls on high-elevation, low-relief landscape formation in the southeast Tibetan Plateau. Geology 50(1):60–65

Zhang Z, Yao H, Yang Y (2020) Shear wave velocity structure of the crust and upper mantle in Southeastern Tibet and its geodynamic implications. Sci China Earth Sci 63:1278–1293

Zhang X, Feng W, Du H, Samsonov S, Yi L (2022a) Super shear rupture during the 2021 MW 7.4 Maduo, China, earthquake. Geophys Res Lett 49:e2022GL097984

Zhang Y, An Y, Long F, Zhu G, Qin M, Zhong Y, Xu Q, Yang H (2022b) Short-term foreshock and aftershock patterns of the 2021 M s 6.4 Yangbi earthquake sequence. Seismol Soc Am 93(1):21–32

Zhao LF, Xie XB, He JK, Tian XB, Yao ZX (2013) Crustal flow pattern beneath the Tibetan Plateau constrained by regional Lg-wave Q tomography. Earth Planet Sci Lett 383:113–122

Zhou L, Song X, Yang X, Zhao C (2020) Rayleigh wave attenuation tomography in the crust of the Chinese Mainland. Geochem Geophys Geosyst 21(8):e2020GC008971

Zheng XF, Yao ZX, Liang JH, Zheng J (2010) The role played and opportunities provided by IGP DMC of China National Seismic Network in Wenchuan earthquake disaster relief and researches. Bull Seismol Soc Am 100(5B):2866–2872.

Publisher's Note